

Direct numerical simulation of nanoparticle coagulation in a temporal mixing layer

S. Modem, S. C. Garrick*, M. R. Zachariah
Department of Mechanical Engineering
University of Minnesota
111 Church Street SE
Minneapolis, MN 55455-0111

K. E. J. Lehtinen
University of Helsinki
Helsinki, 00014 Finland

Corresponding Author: S. C. Garrick
111 Church Street SE
Minneapolis, MN 55455-0111, USA
FAX: (612) 624-5230
e-mail: garrick@me.umn.edu

Colloquium: 1. Combustion Synthesis (MATERIAL-SYNTHESIS)

Word Count: Abstract = 154; body = 2551 + 196 (references) + 2600 (figures) = 5347

April 30, 2002

Abstract

Direct numerical simulations of coagulating aerosols in two-dimensional, mixing layers are performed. The flows consist of the mixing of a particle-laden stream with a particle-free stream, with and without the presence of a temperature gradient. The evolution of the particle field is obtained by utilizing a sectional model to approximate the aerosol general dynamic equation. The sectional model is advantageous in that there are no *a priori* assumptions regarding the particle size distribution. This representation facilitates the capture of the underlying physics in an accurate manner. The growth of particles between $d_p = 1nm$ and $d_p = 10nm$ is captured in both isothermal flows, and flows with a temperature gradient. Results indicate a reduced growth rate in the core of the eddy. The increased temperature of the particle-laden stream results in an increased growth rate. The growth and stretching of the surface area separating the two streams prevents the particle field from achieving the self-preserving particle size distribution.

Introduction

Nanoparticles play a very important role in a wide variety of physical/chemical phenomena and processes. An important application is the synthesis of nanostructured materials. There are several technologies which can be employed in the manufacture of nanoscale materials (films, particles, etc.) Vapor-phase methodologies are by far the most favored because of chemical purity and cost considerations [1]. Gas-phase combustion synthesis is a well proven method for the bulk production of fine powders including silica, titania and carbon black [2, 3, 4, 5, 6]. Nanoparticles also play an integral role in soot formation in combustion systems. Understanding the fundamental processes of soot formation requires knowledge of the precursors, their distribution in space, size and time, their chemical composition, and the underlying hydrodynamic field [7]. These particles typically lie between 1 and 10 nanometers in diameter.

The dynamics of particles in turbulent flows have received some attention. Earlier works focused on understanding the phenomenon of particle dispersion by turbulence [8, 9]. The influence of particle parameters on collision frequencies in a turbulent particle laden suspension leading to coagulation was considered by Sundaram and Collins [10], who showed that the magnitude of the minimum particle collision frequency was strongly correlated with the turbulent motions at the integral scale. Reade and Collins [11] simulated the coagulation and growth of an initially mono-disperse aerosol subject to isotropic turbulence. This work resulted in an improved understanding of the trends in the relative width of the particle size distribution and its dependence on the Stokes number and radial distribution function. However, much of the work performed thus far considered large, micron-scale particles in a Lagrangian manner and utilized primarily particle tracking methods. The large number of particles needed to represent the underlying physics of particle growth using Lagrangian methods render the computations infeasible for all but inhomogeneous systems.

In this work we consider the growth of nanoscale particles in both isothermal and, as typically encountered in combustion environments, non-isothermal temporally developing mixing layers. The particulate phase will be accounted for using a sectional method which treats the particles in an Eulerian manner [12, 13]. This approach is advantageous in that there are no *a priori* assumptions regarding the nature of the particle size distribution. We intend to use direct numerical simulations to capture the underlying physics of particle growth in a model-free manner [14].

Formulation

The flows under consideration are two-dimensional mixing layers and are governed by the compressible Navier-Stokes equations. The transport of the nanoscale particles is governed by the aerosol general dynamic equation (GDE). The GDE is expressed in discrete form as a population balance on each particle size. From a practical standpoint however such systems of equations cannot be solved explicitly except for very small particle sizes. To overcome this a sectional method is used to represent the particle field [15, 16, 17]. This approach effectively divides the particle size distribution into “bins.” We consider only large clusters and particles which typically contain tens of thousands of molecules, for which a discrete or molecular cluster representation is unnecessary. The GDE is therefore solved as a set of N_s transport equations, one for each section Q_k , $k = 1, 2, \dots, N_s$ [18]. In adopting this framework we can write the general transport equation for the concentration of particles in the k th section, Q_k as

$$\frac{\partial \rho Q_k}{\partial t} + \frac{\partial \rho Q_k u_j}{\partial x_j} = \frac{\partial}{\partial x_j} \left(\mathcal{D}_{Q_k} \frac{\partial Q_k}{\partial x_j} \right) + \omega_k^Q, \quad (1)$$

where \mathcal{D}_Q is the diffusivity of a particle in section k , and is given by

$$\mathcal{D}_{Q_k} = k_b T \frac{C_c}{3\pi\mu d_p}, \quad (2)$$

where k_b is the Boltzmann constant, C_c is the Cunningham correction factor, d_p is the particle diameter, μ is the fluid viscosity and T is the fluid temperature [19, 20, 21]. The source term, ω_k^Q , is given by

$$\omega_k^Q = \frac{1}{2} \sum_{i=1}^{N_s} \sum_{j=1}^{N_s} \beta_{ij} \chi_{ijk} Q_i Q_j - \sum_{i=1}^{N_s} \beta_{ik} Q_i Q_k, \quad (3)$$

and represents the effect of particle-particle interactions resulting in coagulation: production of Q_k due to collisions of smaller particles; the loss or gain of Q_k by collision with a smaller particle which either moves the resulting particle out of or into section k ; the loss of particles in section k as they collide with each other and form larger particles; and the loss of particles in section k due to collisions with larger particles. It should be noted that repeated indices in Eq. (3) do not imply summation but instead infer interactions between particles in section i and particles in section j . The collision frequency function β_{ij} is that for Brownian coagulation and is given by

$$\beta_{ij} = \left(\frac{3}{4\pi}\right)^{\frac{1}{6}} \left(\frac{6k_bT}{\rho_p}\right)^{\frac{1}{2}} \left(\frac{1}{v_i} + \frac{1}{v_j}\right)^{\frac{1}{2}} \left(v_i^{\frac{1}{3}} + v_j^{\frac{1}{3}}\right)^2, \quad (4)$$

where v_i is the volume of the i th particle, ρ_p is the particle density and χ_{ijk} is given by

$$\chi_{ijk} = \begin{cases} \frac{v_{k+1} - (v_i + v_j)}{v_{k+1} - v_k} & \text{if } v_k \leq v_i + v_j < v_{k+1} \\ \frac{(v_i + v_j) - v_{k-1}}{v_k - v_{k-1}} & \text{if } v_{k-1} \leq v_i + v_j < v_k \\ 0 & \text{otherwise.} \end{cases} \quad (5)$$

The sectional method is discretized in size space such that the volume of particles is doubled between two successive sections, i.e. $v_k = 2 \times v_{k-1}$. This scheme allows us to span a volume range of $V = v_1$ to $V = 2^{N_s-1} \times v_1$.

Results

The flows under consideration are two-dimensional mixing layers, a schematic of which is shown in Fig. 1. The Reynolds number is based on the initial vorticity thickness $L = \delta_{\omega_0}$, the velocity difference across the mixing layer $U_o = (U_1 - U_2)/2$ and the value for all flows considered is $Re = U_o L / \nu = 200$. Initially, the upper stream (stream 1) is free of particles, while the lower stream (stream 2) is populated by $d_p = 1nm$ sized particles (contained within section 1). A total of twelve sections are solved for, i.e. $N_s = 12$. This allows for the solution of particles covering a range of 3 orders of magnitude in volume, or a diameter range of $1 \leq d_p \leq 10nm$. To elucidate the effects of temperature, two cases are considered: Case (I) considers an isothermal mixing layer where $T_1 = T_2 = 300K$, and Case (II) considers a temperature gradient across the mixing layer in which $T_2 = 3 \times T_1 = 900K$. The volume fraction, defined as the ratio of the volume occupied by the particulate phase to that occupied by the fluid, is $\Phi = 9.4 \times 10^{-8}$ for both cases.

Computations are performed on a domain of $2\pi \times 2\pi$ in the streamwise and cross-stream directions on a mesh consisting of $1,500 \times 1,500$ points and each calculation simulated up to a non-dimensional time of $t^* = U_o t / \delta_{\omega_0} = 14.25$. The governing transport equations are solved using a hybrid MacCormack based compact difference scheme [22, 23]. The numerical scheme used is based on the one-parameter family of dissipative two-four schemes [22]. The accuracy of the scheme is second order in time, and fourth order in space. All calculations are performed on a uniformly spaced, rectangular grid.

Instantaneous and spatially-averaged concentration data are presented to aid in making both qualitative and quantitative assessments of the temporal evolution and spatial structure of the particulate field. Concentration profiles are obtained by averaging over the ‘‘homogeneous’’ x-direction and therefore contain 1,500 samples. All average quantities are denoted with an over-bar. Additionally, all particle concentrations are normalized by the initial number of particles in section 1, $Q_{1,o}$, and are denoted Q_k^* , i.e. $Q_k^* = Q_k / Q_{1,o}$. At time $t^* = 0$, the concentration is $Q_1^* = 0$ in the particle-free stream and $Q_1^* = 1$ in the particle-laden stream. For purposes of characterizing the mixing layer growth the vorticity thickness δ_{ω_0} is used. The vorticity thickness is a measure of the width of the mixing layer, and is defined as twice the 90% width of the u-velocity, u . The growth rate of the temporal mixing layer is shown Fig. 2. The evolution of the vorticity thickness for Case (I) and Case (II) reveals that the growth rate of the mixing layer is reduced in the presence of a temperature gradient. The maximum thickness in Case (I) is more than twice that of Case (II). This reduced growth or spread of the eddy means that less of the fluid emanating from the ‘‘free-stream’’ regions will be engulfed in the core. Such diminished growth rates have been previously observed [24, 25] and is shown here to demonstrate the effect of the temperature gradient on the hydrodynamic field.

Cross-stream profiles of the $1nm$ and $4nm$ diameter particle concentrations are shown in Fig. 3. As the mixing layer evolves the particle-laden stream is mixed with the particle-free fluid. As the particles collide, they coagulate to form larger particles and thereby move out of section 1 and into higher numbered sections, $Q_k, k = 2, 3, \dots, 10$. The profiles contained within Fig. 3(a) reveal that the number of $d_p = 1nm$ particles decreases with time for both Case (I) and Case (II), with the rate of decrease being higher in Case (II). This increased growth rate reflects the temperature-dependent collision frequency function, Eq. (4). The collision rate of particles in Case (II) is increased by a factor of $3^{1/2}$ over that in Case (I). A similar trend is observed in the region near the interface of the two streams. The growth rate in the core of the eddy is less than that in the particle-laden stream. This is the result of two physical mechanisms. The higher temperature of the particle-laden stream in Case (II) increases the growth rate by increasing the rate of collisions β_{ij} . Additionally, in this region, the particle-free and particle-laden streams mix thereby diluting the concentration of particles which reduces the growth rate. The eddy grows less in Case (II), as shown in Fig. 2, which results in a reduced dilution of the particle-laden fluid, thereby increasing the growth rate in the particle-laden stream. The concentration of $4nm$ diameter particles is shown in Fig. 3(b). The trend in the cross-stream profiles is different from that observed in the first section in that the maximum concentration is observed in the initially particle-laden stream at all times. The particle concentration increases from zero to a value of $\overline{Q}_7^* = 0.0032$ at $t^* = 3.40$, reaches a maximum value of $\overline{Q}_7^* = 0.0043$ at $t^* = 6.01$ and then decreases to $\overline{Q}_7^* = 0.0039$ at $t^* = 9.13$. Over the same time interval, the concentrations in Case (II), are $\overline{Q}_7^* = 0.0014$, $\overline{Q}_7^* = 0.0012$, and $\overline{Q}_7^* = 0.0008$. This monotonic decrease of particles in the particle-laden stream represents the increased growth rate occurring in Case (II); the concentration of $d_p = 4nm$ particles has reached its maximum value earlier than in Case (I). Near the interface of the two streams the trend is different from that observed in the smaller-diameter section 1 particles. Near $y/\pi = 0$, the concentration increases to a particular value and tends to remain constant over the observed time interval. This quasi-equilibrium value is $\overline{Q}_7^* = 0.0019$ in Case (I) and is $\overline{Q}_7^* = 0.0008$ in Case (II).

A qualitative view of the particle field for the isothermal flow, Case (I), is presented in Fig. 4. This figure shows instantaneous contours of the 2 and $8nm$ diameter particle concentration at time $t^* = 9.13$. There is noticeable spatial segregation of the various particles: the highest concentration of $d_p = 1nm$ particles exist in a band between the initially particle-free and particle-laden stream; the highest concentration of $d_p = 2nm$ particles are contained within the core of the eddy while the concentration in the particle-laden stream is roughly 50% of the maximum value; the highest concentration of $d_p = 4nm$ particles are in the freestream while the eddy core contains particles at concentration levels between 30 and 70 percent of the maximum; and the highest concentration of $d_p = 8nm$ particles also occurs in the freestream while the eddy core is essentially devoid of the larger particles. This structure further underscores the reduced growth rate occurring in the eddy core. In addition to spatial concentration variation, the effects of differential diffusion are also evident. The striation thickness decreases as the particle size increases. This is because larger particles have smaller coefficients of diffusion.

The overall effect of the temperature gradient can be characterized by considering the mean particle size. The mean diameter is given by $\overline{d}_p = (6/\pi\overline{v})^{1/3}$, where the mean volume is given by

$$\overline{v} = \frac{\sum_{i=1}^{N_s} Q_i v_i}{\sum_{i=1}^{N_s} Q_i}. \quad (6)$$

The temporal evolution of the mean diameter for Case (I) and Case (II) is shown in Fig. 5. The mean diameter is maximum in the initially particle laden stream and decreases gradually to zero in the particle free stream. Though the profiles show an overall increase with time, the particle growth rate in Case (II) is higher than that in Case (I) at all times. Additionally, the mean diameter is lower in the core of the eddy in both cases. At the interface of the two streams, $y/\pi = 0$, the mean diameter in Case (I) increases to $\overline{d}_p = 1.85nm$ at $t^* = 3.40$, $\overline{d}_p = 2.15nm$ at $t^* = 6.01$ and $\overline{d}_p = 2.22nm$ at $t^* = 9.13$, whereas in Case (II) the mean diameter is $\overline{d}_p = 2.40nm$ at $t^* = 3.40$, $\overline{d}_p = 2.81nm$ and $\overline{d}_p = 3.25nm$ at the same times. Figure 6 shows the spatially resolved mean diameter d_p geometric standard deviation σ_g at time $t^* = 9.13$. The lower stream contains the largest particles and the diameter and variance are consistent with a homogeneous flow of coagulating aerosols. The largest particles are found in the freestream region of the particle-laden stream, and the variance of $\sigma_g = 1.5$ indicates the self-preserving limit found for coagulating aerosols using a finite number of sections [12]. The smallest particles are found at the farthest outer edge of the shear interface. These particles remain small because they preferentially diffuse to the particle-free region where the lower concentration also lowers the overall growth rate, which in turn preserves their size. In fact, the particles in the shear layer have a size

distribution smaller than self-preserving ($\sigma_g < 1.5$), indicating that the characteristic time for transport is faster than coagulation. These gradients in size and number concentration get magnified further during the formation of the eddy. The material in the eddy is always of average or smaller size than the particle-laden stream. As the eddy develops and increases the available shear layer surface area, a larger fraction of particles undergo diffusive transport and diminished rate of coagulation. Eventually as the shear layer “wraps around,” we find regions where diffusion effects increase the width of the size distribution over that in the self-preserving limit.

Conclusions

In the present work we utilized a sectional methodology to perform DNS of nanoparticle coagulation in both isothermal and non-isothermal temporal mixing layers. The particulate field was obtained as a function of size, space and time. Results indicate that the growth rate of the particles in the freestream region of the particle-laden stream is greater than that in the core of the eddy. The growth of the particles was enhanced by the presence of the higher temperature stream due to the increased collision frequency. Additionally, by considering both the mean diameter and the variance, we are able to quantify the effects of convection and diffusion on disturbing the particle size distribution away from self-preserving behavior. The regions of the flow where $\sigma_g \neq 1.5$ indicates that methodologies which assume a self-preserving distribution may not perform very well in representing particle coagulation in shear flows. This work demonstrates the viability of the sectional method in capturing the growth of nanoscale particles. The methodology is sufficiently general to allow for the inclusion of phenomena such as nucleation, condensation, evaporation, thermophoresis and other fluid-particle interactions.

Acknowledgment

The first two authors acknowledge the support of the National Science Foundation under Grant ACI-9982274. Computational resources are provided by the Minnesota Supercomputing Institute.

References

- [1] Pratsinis, S. E., *Prog. Energy Combust. Sci.*, **24**:197 (1998).
- [2] Ulrich, G. D. and Subramanian, N. S., *Combust. Sci. and Tech.*, **18**:119–126 (1977).
- [3] Ulrich, G., *Chem. Eng. News*, (1994).
- [4] Zachariah, M. R., Aquino-Class, M., and Shull, R. D., *Nanostructured Materials*, **5**:383 (1995).
- [5] Vemury, S., Pratsinis, S., and Kibbey, L., *J. Mat. Res.*, **12**:1031 (1997).
- [6] Wooldridge, M. S., *Prog. Energy Combust. Sci.*, **24**:63 (1998).
- [7] Lin, K. C. and Faeth, G. M., in *Proc. Spring Technical Meeting of the Combustion Institute, Central States Section*, Pittsburgh, PA, 1994.
- [8] Riley, J. J. and Patterson, G. S., *Phys. Fluids*, **17**:292–297 (1974).
- [9] Elghobashi, S., *Appl.Sci.Res.*, **48**:301–314 (1991).
- [10] Sundaram, S. and Collins, L. R., *J. Fluid Mech.*, **335**:75–109 (1996).
- [11] Reade, W. C. and Collins, L. R., *J. Fluid Mech.*, **415**:45–64 (2000).
- [12] Pyykonen, J. and Jokiniemi, J., *J. Aerosol Sci.*, **31**(5):531–550 (2000).
- [13] Garrick, S. C., Lehtinen, K. E. J., and Zachariah, M. R., in *Proc. Joint US Sections Meeting of the Combustion Institute*, Oakland, CA, 2001.
- [14] Givi, P., *Prog. Energy Combust. Sci.*, **15**:1–107 (1989).
- [15] Gelbhard, F. and Seinfeld, J. H., *Coll. Int. Sci.*, **78**:485–501 (1980).
- [16] Gelbhard, F., Tambour, Y., and Seinfeld, J. H., *Coll. Int. Sci.*, **76**:541–556 (1980).
- [17] Landgrebe, J. D. and Pratsinis, S. E., *Coll. Int. Sci.*, **139**:63–85 (1990).
- [18] Xiong, Y. and Pratsinis, E. S., *J. Aerosol Sci.*, **24**(3):283–300 (1993).
- [19] Fuchs, N. A., *The Mechanics of Aerosols*, Pergamon, Oxford, England, 1964.
- [20] Friedlander, S. K., *Smoke, Dust and Haze: Fundamentals of Aerosol Behavior*, John Wiley and Sons, New York, NY, 1977.
- [21] Matsoukas, T. and Friedlander, S. K., *Coll. Int. Sci.*, **146** (1991).
- [22] Carpenter, M. H., in Morton, K. W., editor, *Twelfth International Conference on Numerical Methods in Fluid Dynamics, Lecture Notes in Physics*, Vol. 371, pp. 254–258, Springer-Verlag, New York, NY, 1990.
- [23] Kennedy, C. A. and Carpenter, M. H., *Appl. Num. Math.*, **14**:397–433 (1994).
- [24] Sandham, N. D. and Reynolds, W. C., *J. Fluid Mech.*, **224**:133–158 (1991).
- [25] Givi, P., Madnia, C. K., Steinberger, C. J., Carpenter, M. H., and Drummond, J. P., *Combust. Sci. and Tech.*, **78**:33–68 (1991).

List of Figures

1	Temporal mixing layer configuration.	9
2	Temporal evolution of vorticity thickness, δ_ω	9
3	Cross stream variation of particle concentrations: (a) $\overline{Q_1^*}$; (b) $\overline{Q_7^*}$	9
4	Instantaneous particle concentrations contours, Case (I): (a) Q_1^* (b) Q_4^* (c) Q_7^* (d) Q_{10}^*	10
5	Cross stream variation of the mean particle diameter $\overline{d_p}$	10
6	Instantaneous contours of mean diameter d_p and geometric standard deviation σ_g at time $t^* = 9.13$: (a) d_p Case (I); (b) σ_g Case (I); (c) d_p Case (II); (d) σ_g Case (II).	11

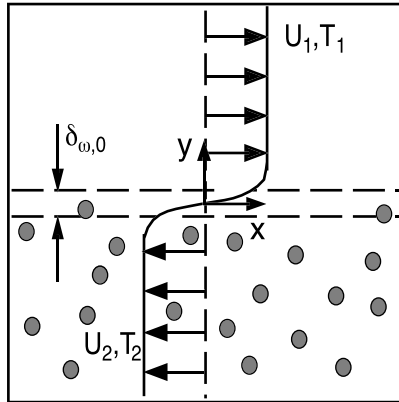


Figure 1: Temporal mixing layer configuration.

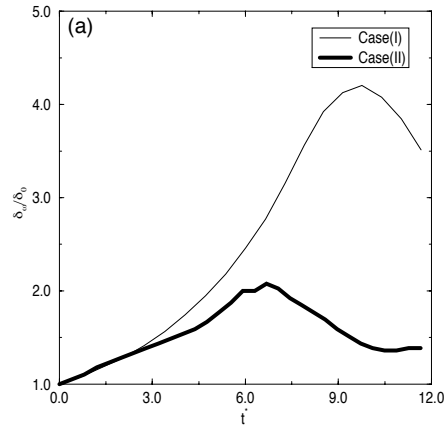


Figure 2: Temporal evolution of vorticity thickness, δ_ω .

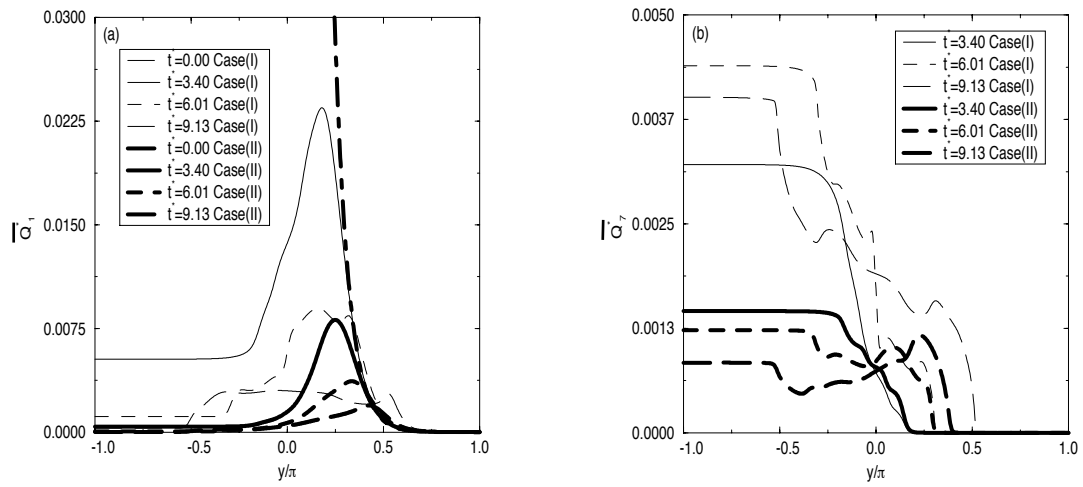


Figure 3: Cross stream variation of particle concentrations: (a) $\overline{Q_1^*}$; (b) $\overline{Q_7^*}$.

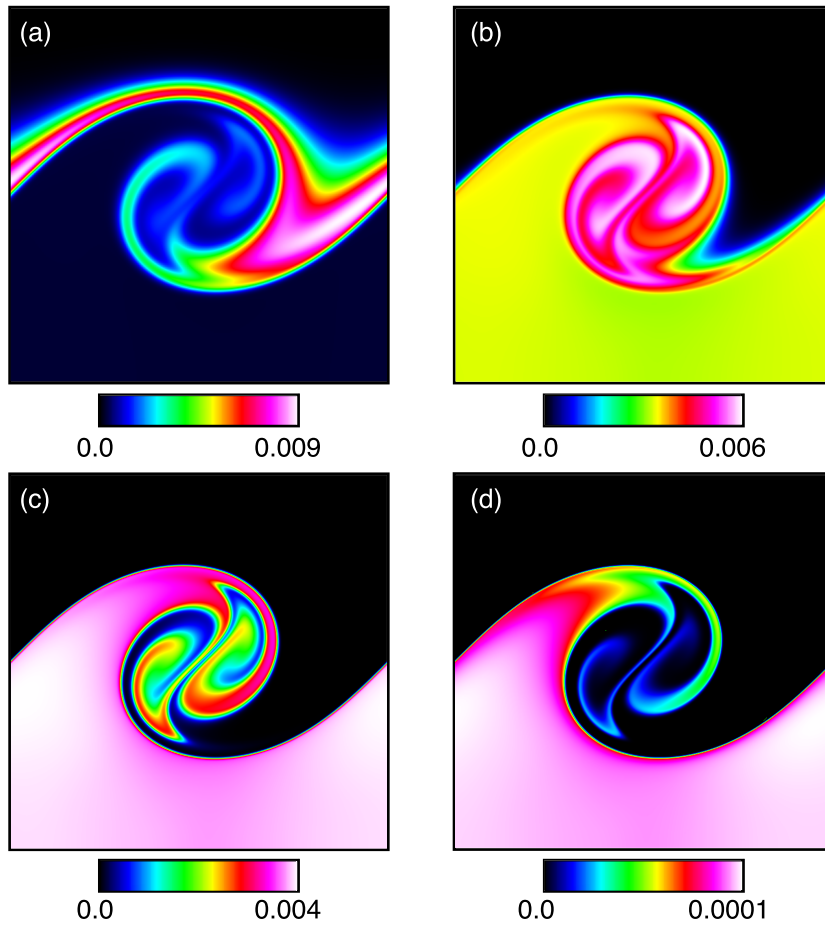


Figure 4: Instantaneous particle concentrations contours, Case (I): (a) Q_1^* (b) Q_4^* (c) Q_7^* (d) Q_{10}^*

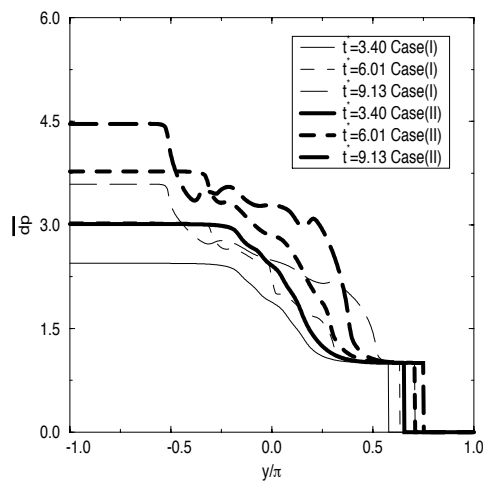


Figure 5: Cross stream variation of the mean particle diameter \bar{d}_p .

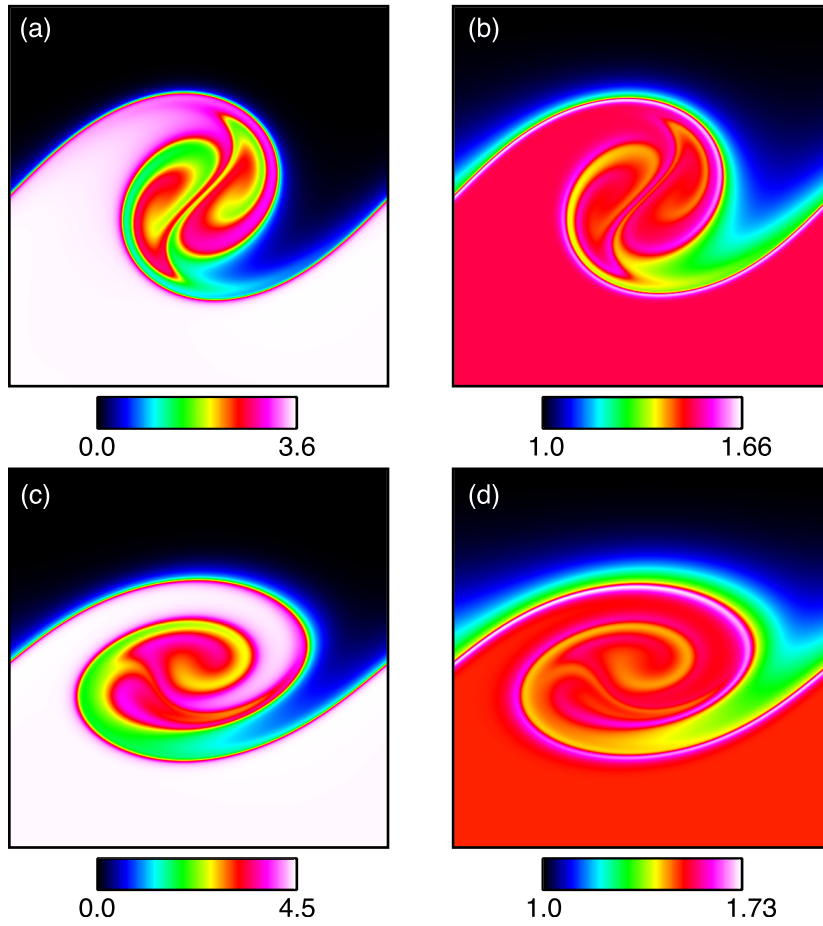


Figure 6: Instantaneous contours of mean diameter d_p and geometric standard deviation σ_g at time $t^* = 9.13$: (a) d_p Case (I); (b) σ_g Case (I); (c) d_p Case (II); (d) σ_g Case (II).